#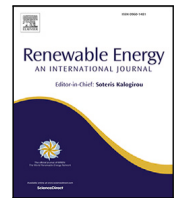 Performance characteristics of a contra-rotating pump-turbine in turbine and pump modes under cavitating flow conditions

N.B. When citing this work, cite the original published paper.

(article starts on next page)

Performance characteristics of a contra-rotating pump-turbine in turbine and pump modes under cavitating flow conditions

Jonathan Fahlbeck [a,*], Håkan Nilsson [a], Mohammad Hossein Arabnejad [a], Saeed Salehi [a,b]

[a] *Department of Mechanics and Maritime Sciences, Chalmers University of Technology, Gothenburg SE 412 96, Sweden*
[b] *Chalmers Industriteknik, Gothenburg SE 412 58, Sweden*

ARTICLE INFO

ABSTRACT

Recent studies have indicated the potential of a contra-rotating pump-turbine (CRPT) as a low-head design that enables pumped hydro storage in regions with flat topography. However, the effects of cavitation have scarcely been investigated for the CRPT. The current paper utilises computational fluid dynamics simulations to study a model scale CRPT subjected to cavitating flow conditions to determine how cavitation affects the machine's operating performance in both pump and turbine modes. In total, eight operating conditions have been evaluated for each mode. The inlet flow rate is considered fixed at 0.27 m³/s, while the outlet pressure is gradually changed to induce cavitating conditions. The study demonstrates that the pump mode operation of the CRPT is more sensitive to cavitation compared to the turbine mode. The pump mode operation shows a steady decline in efficiency with decreasing inlet pressure, whereas in turbine mode the efficiency settles at a lower level. The 3% head drop occurs at a Thoma number of 1.0 in pump mode and at 0.6 in turbine mode. At the 3% head drop, a large cavitating region is already present at the runner blades' suction side of the runner closest to the lower reservoir in both modes. The large cavitating region causes the flow to separate from the runner blade surfaces, which explains the reduced operating performance. To ensure an almost cavitating-free operating condition and unaffected performance, the Thoma number needs to be above 1.0 in turbine mode and at least 1.5 in pump mode. A frequency analysis reveals that the presence of cavitation affects the dominant pressure pulsations in the system. A dynamic mode decomposition analysis is carried out, demonstrating that the non-trivial pressure pulsations are connected to the support struts.

1. Introduction

The increasing share of intermittent energy sources for the production of electrical energy has highlighted the need for more effective energy storage. Pumped hydro storage (PHS) currently stands as the most common type of energy storage [1]. The development of PHS has primarily focused on high-head applications imposing constraints on its geographical feasibility and utilisation [2]. To expand the applicability of PHS to regions or countries where construction of high-head PHS facilities may not be feasible, the ALPHEUS (augmenting grid stability through low-head pumped hydro energy utilization and storage) EU H2020 project [3,4] was established. As a part of the project, novel runner designs for low-head applications (between 2 to 20 m) were developed. Specifically, a model scale shaft-driven contra-rotating pump-turbine (CRPT) has been designed.

A CRPT is an axial flow machine that has two individual runners rotating in opposite directions. Axial flow machines are suitable in low-head scenarios since they operate at higher flow rates compared to mixed or radial-flow machines. A high flow rate is desirable at low-head sites because the power is proportional to the head and flow rate [5]. The main advantage of a CRPT compared to a single runner configuration is that it allows for a wider operating range at high efficiency according to Furukawa et al. [6]. Furthermore, they stated that a CRPT has a flatter head-flow rate curve which makes it suitable for low-head PHS since the relative variation in the head is much larger compared to high-head scenarios.

Extensive numerical studies of the model scale CRPT in the ALPHEUS project have previously been carried out [7–9]. These studies predominantly concern non-cavitating transient operations of the machine. However, it has been demonstrated in the literature [10,11] that cavitation can significantly degrade the operating capabilities of pump-turbines. Therefore, it is crucial to analyse the CRPT at a wide range of operating conditions, in both pump and turbine modes, to comprehend how the machine is potentially affected by cavitation. Cao et al. [12]
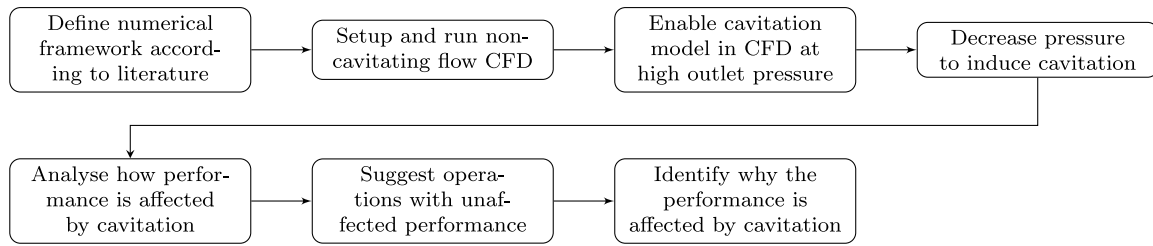

Fig. 1. Flow chart of study and research objectives.

briefly mentioned that their tested CRPT had improved cavitation characteristics compared to a conventional single-runner machine. In an experimental study, the same research group showed that cavitation inception occurred at the tip of the leading edge of the rear runner [6]. For that reason, they redesigned the rear runner for a lower rotational speed to avoid cavitation [13]. When they redesigned the rear runner, only single-phase flows were considered and no analysis where made that could capture cavitation. The CRPT has furthermore been experimentally studied under air/water two-phase flow conditions by increasing the airflow rate of an air–water mixture [6,14] However, no thorough study on how cavitation affects the operating performance of a CRPT is found in the literature. Therefore, this study aims to numerically examine and explain how cavitation impacts the operating performance of the CRPT at stationary conditions.

In 1998, Hirschi et al. [15] reported that 3D computational fluid dynamics (CFD) simulations of cavitating flow, together with the Rayleigh–Plesset equation, compared rather well with measured data for a centrifugal impeller. Additionally, Lei et al. [16] demonstrated the effectiveness of CFD simulations in capturing the physics of cavitating regions, even under off-design conditions for a centrifugal pump. In their study, they utilised the RNG k-ε Reynolds-averaged Navier–Stokes (RANS) simulations together with a homogeneous mixture model. Another investigation focused on cavitating flow in an axial flow pump, with CFD results being compared to experimental data [17]. The numerical framework incorporated a two-phase mixture model and a RANS turbulence model, and it was shown that the simulations were in agreement with the measured data. Likewise, axial flow turbines have been studied under cavitating flow conditions [18] using similar numerical methods as in the previously listed studies. It was shown that for the axial flow turbine, the tip clearance region is where cavitation is likely to be formed because of the large difference in pressure between the pressure and suction sides of the runner. Furthermore, the potential of the Schnerr–Sauer model for accurately capturing phase change in the OpenFOAM open-source CFD code has been demonstrated [19,20]. These studies demonstrate that CFD simulations can be used to accurately predict the operating performance for a wide range of hydraulic machines under cavitating flow conditions.

Similar to the previous studies, the present work utilises CFD simulations with a two-phase mixture model to capture cavitation while here applied to the model scale CRPT developed in the ALPHEUS project. The objective is to understand how cavitation affects the CRPT's operating performance and identify potential operating conditions that limit cavitation. Consequently, a wide range of operating conditions is assessed numerically both in turbine and pump modes by changing the outlet pressure of the machine. The findings of this study hold significance when planning for future low-head PSH projects and offer valuable insights to ensure the safe and optimal operation of the CRPT. This study is outlined according to Fig. 1 and the paper is structured as follows. Section 2 provides an explanation of the runner design and operating conditions. This is followed by a description of the numerical framework in Section 3. The results are then discussed in Section 4. First, a general comparison of both modes is provided, followed by a detailed study of cavitating flow conditions in turbine mode and subsequently in pump mode. Finally, the conclusions from this work are presented in Section 5.

2. Runner design and operating conditions

The numerical domain of the studied CRPT and its mounting arrangement is depicted in Fig. 2. The mounting arrangement was designed within the ALPHEUS project to manage the loads and constraints of the experimental test facility where the machine is tested. The blade geometries of the runners were designed and optimised to maximise the efficiency at a wide range of operating conditions. The runners (shown in red and blue colours) are connected to individual shafts to transmit the torque to/from individual motor-generator units. The axial shaft of each runner is connected to a vertical shaft placed in one of the larger support struts via a set of bevel gears. More information about the configuration of the test facility is provided by Hoffstaedt et al. [21]. The set of smaller support struts, closer to the runners, are required for structural integrity. Runner 1 (red) has eight blades and is located upstream in pump mode, and downstream in turbine mode while Runner 2 (blue) has seven blades. The tip diameter of the CRPT is 276 mm, the hub diameter is 124 mm, and a tip clearance of 0.68 mm is used between the runner tip and the shroud.

The evaluated operating conditions are based on keeping the flow rate of the machine constant at 0.27 m^3/s while achieving comparably high hydraulic efficiencies. The flow rate of 0.27 m^3/s is loosely based on what should be achievable in future lab tests in both modes. In turbine mode, Runner 1 rotates at 842 rpm and Runner 2 at 633 rpm. In pump mode, a higher rotational speed is needed to achieve an appropriate hydraulic efficiency. Consequently, the Runner 1 speed is set to 1129 rpm while Runner 2 rotates at 848 rpm. The prescribed rotational speeds yield the same rotational speed ratio of the runners of 0.75 in both pump and turbine modes. In the case of a non-cavitating flow, these operating conditions correspond to a hydraulic efficiency of 90% in turbine mode and 86% in pump mode. In turbine mode, each of the runners is responsible for roughly 50% of the net head and power. This is in contrast to the pump mode where Runner 1 is responsible for about 58% of the net head and 57% of the power of the full CRPT.

The performance parameters evaluated in this work are primarily the net head (H), power (P) and hydraulic efficiency (η) of the CRPT. These parameters are defined as

$$H = \frac{\Delta p_0}{\rho g}, \tag{1}$$

$$P = \sum_{i=1}^{2} T_{\mathrm{R}i} \Omega_{\mathrm{R}i}, \tag{2}$$

$$\eta_{\mathrm{T}} = \frac{P}{\rho g H Q}, \quad \eta_{\mathrm{P}} = \frac{\rho g H Q}{P}, \tag{3}$$

where Δp_0 is the total pressure change over the runners, ρ is the fluid density, g is the gravitational acceleration, and Q is the volumetric flow rate. The torque and rotational speed of each runner are denoted by $T_{\mathrm{R}i}$ and $\Omega_{\mathrm{R}i}$, where index i is 1 or 2 for the respective runner. Subscript T is for turbine mode, and P is for pump mode. To evaluate the cavitation condition, the Thoma number (σ) is considered according to IEC 60193 [22] as

$$\sigma = \frac{\mathrm{NPSE}}{\mathrm{E}} = \frac{\frac{p_{\mathrm{LP}} - p_{\mathrm{v}}}{\rho} + \frac{Q^2}{2 A_{\mathrm{LP}}^2}}{g H}. \tag{4}$$

(a) Full computational domain

P3$_{\text{pos}}$

(b) Zoom in by the runners and mounting arrangement
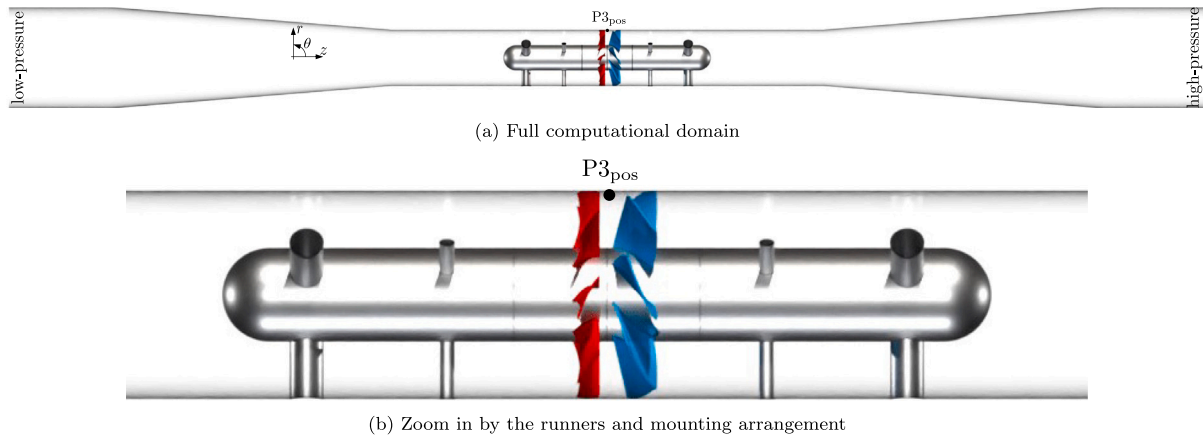
Fig. 2. Computational domain with the pressure probe P3$_{\text{pos}}$ location and coordinate system. Runner 1 is red and Runner 2 is blue, the flow is from right to left in turbine mode, and from left to right in pump mode.

Here p_{LP} and A_{LP} are the static pressure and the cross-sectional area at the low-pressure boundary of the computational domain (see Fig. 2(a)), respectively, while p_{v} is the vapour pressure. In turbine mode, p_{LP} is directly specified since it is the outflow boundary. On the contrary in pump mode, the pressure is set at the high-pressure boundary. The specified outflow pressure is changed to evaluate the CRPT at various Thoma numbers. The largest outflow pressure is set so that the Thoma number is around 2.0 in both modes. This yields the largest outflow pressure of 115 kPa in turbine mode and 220 kPa in pump mode.

3. Method

This section presents the methods used to carry out the numerical simulations. First, the solver settings and mesh are explained, followed by a description of the cavitation model, and finally the boundary conditions are presented.

3.1. Numerical setup and mesh

The OpenFOAM-v2112 [23] open-source CFD code is used for the simulations. In the cavitating flow simulations, the OpenFOAM interPhaseChangeDyMFoam solver is used. That solver treats the fluid as a mixture of two incompressible and isothermal fluids and allows for phase change, as described in Section 3.2. Thus, the Navier–Stokes equations are solved for the mixture, and an arbitrary mixture quantity (*e.g.* $\rho_{\text{m}}, \mu_{\text{m}}$) is calculated as

$$\phi_{\text{m}} = \sum_{i=1}^{2} \alpha_i \phi_i, \tag{5}$$

where α_i is the volume fraction of phase i (here liquid or vapour).

In the present study, the RANS equations are solved using the k-ω SST-SAS (shear stress transport — scale adaptive simulation) turbulence model [24,25]. The model uses a hybrid RANS approach through an additional source term in the ω transport equation that detects turbulence and reduces the turbulent viscosity in parts of the numerical domain. Hence, turbulence is partly resolved in the simulations. The turbulence model has recently been used in several studies of hydro machines with sufficiently accurate results [26–28].

The discretisation schemes are second-order accurate, except that the convective terms of the k, ω and α_l (liquid volume fraction) equations are discretised using the first-order upwind scheme. The convective terms in the momentum equations are discretised using the LUST (linear-upwind stabilised transport) scheme [29]. The LUST scheme utilises 75% of the central difference scheme for accuracy and 25% of a second-order upwind scheme for stability. Temporal terms are discretised with the second-order backward scheme [30] with a fixed

time step. In turbine mode the time step is set to 5×10^{-5} s (maximum of 0.25°per time step). In pump mode a time step of 2.5×10^{-5} s (maximum of 0.17°per time step) is used because of the higher runner rotational speed.

The interPhaseChangeDyMFoam solver couples pressure and velocity through the PIMPLE algorithm [31], which is a combination of the SIMPLE [32] and PISO [33] algorithms. PIMPLE is basically an outer SIMPLE loop on top of the inner PISO algorithm. In the cavitating flow simulations, three inner loops and one non-orthogonal corrector step are performed within each outer loop. The convergence criterion is set to a solver residual of 10^{-6} for pressure and velocity, which is usually reached within four to six outer loops.

The most essential parts of the numerical mesh are shown in the mesh cut view in Fig. 3. The mesh is divided into four parts, one for each of the runners, and the two regions containing the straight parts and the contraction/expansion upstream and downstream of the CRPT. The mesh is finest at the runners and is gradually coarser away from the runners. The runner mesh regions are block-structured, except in the tip-clearance region where nine layers of hexahedral and triangular prism cells are used. The two runner mesh regions contain about 2×10^6 cells each. The upstream and downstream sections are identical and thus only one of them is presented in Fig. 3. The mesh is constructed with an unstructured tetrahedral core and ten prism layer boundary cells. The corresponding mesh consists of approximately 4×10^6 cells. This gives a total cell count of 12×10^6 cells for the complete computational domain. A mesh study has been carried out in our previous work [7], using a mesh with almost identical properties. It was shown that the expected relative error of the computed power was less than 1%, which is considered sufficient for the present study.

3.2. Cavitation model

Cavitation is in this study modelled using the Schnerr–Sauer model [34–36]. A transport equation for the liquid volume fraction is solved [19], reading

$$\frac{\partial}{\partial t}(\alpha_l \rho_l) + \frac{\partial}{\partial x_i}(u_i \alpha_l \rho_l) = \dot{m}, \tag{6}$$

where α_l is the liquid volume fraction, ρ_l is the liquid density, u is the mixture velocity, and subscript i denotes the Cartesian directions. The mass transfer term $\dot{m}$ accounts for vaporisation and condensation processes. The mass transfer is in the Schnerr–Sauer model [35] written as the summation of vaporisation ($\dot{m}_{\alpha_{l,V}}$) and condensation ($\dot{m}_{\alpha_{l,C}}$) terms as

$$\dot{m} = \alpha_l(\dot{m}_{\alpha_{l,V}} - \dot{m}_{\alpha_{l,C}}) + \dot{m}_{\alpha_{l,C}}, \tag{7}$$
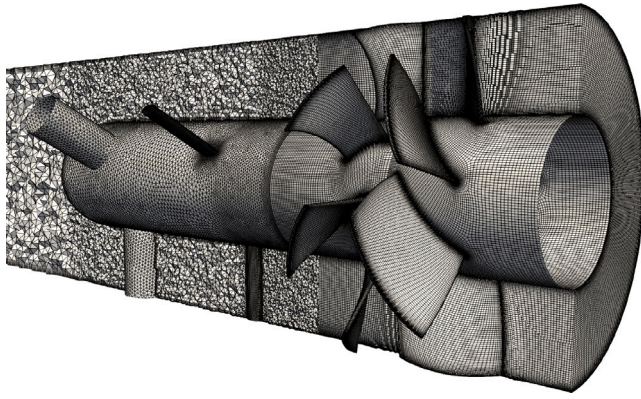
Fig. 3. Cross-sectional view of the employed mesh around the runners and the support struts. Only one set of support struts is shown due to their similarity.

where

$$\dot{m}_{\alpha_{l,V}} = C_V(1 + \alpha_{Nuc} - \alpha_l)\frac{3\rho_l\rho_v}{\rho R_B}\sqrt{\frac{2}{3\rho_l}}\sqrt{\frac{1}{|p - p_v|}}\min(p - p_v, 0), \quad (8)$$

$$\dot{m}_{\alpha_{l,C}} = C_C\alpha_l\frac{3\rho_l\rho_v}{\rho R_B}\sqrt{\frac{2}{3\rho_l}}\sqrt{\frac{1}{|p - p_v|}}\max(p - p_v, 0). \quad (9)$$

Here, C_V and C_C are vaporisation and condensation coefficients which are set to one during the cavitating flow simulations. p and p_v are the local and vapour pressures, respectively. The vapour pressure is here assumed to be 2340 Pa, which is the vapour pressure for water at 20 °C. The bubble radius is obtained through

$$R_B = \sqrt[3]{\frac{3}{4\pi n_0}\frac{1 + \alpha_{Nuc} - \alpha_l}{\alpha_l}}, \quad (10)$$

and the initial nuclei volume fraction is defined as [36]

$$\alpha_{Nuc} = \frac{V_{Nuc}}{V_{cell}} = \frac{n_0\frac{4}{3}\pi R_{Nuc}^3}{1 + n_0\frac{4}{3}\pi R_{Nuc}^3}. \quad (11)$$

Here, V_{Nuc} is the volume of nuclei in a cell with the cell volume V_{cell}, n_0 is the nuclei density, which is the number of nuclei per unit volume of liquid. In this work, the initial nuclei density and the nuclei radius have assumed values of $n_0 = 10^{12}$ nuclei/m³ and $R_{Nuc} = 5 \times 10^{-6}$ m, respectively. This means that if a cell has no vapour ($\alpha_l = 1$), there is $n_0 \times V_{cell}$ number of small bubbles with the nuclei radius R_{Nuc} within the cell, otherwise the bubble radius is obtained through Eq. (10).

3.3. Boundary conditions

The boundary conditions are set by prescribing a fixed volumetric flow rate at the inlet of 0.27 m³/s and a uniform static pressure at the outlet boundary. In turbine mode the high-pressure boundary is the inlet whereas it is the outlet boundary in pump mode, see Fig. 2(a). To evaluate the CRPT at different Thoma numbers, corresponding to different cavitation conditions, the static outlet pressure is varied. In turbine mode, the specified pressure at the low-pressure boundary ranges between 10–115 kPa. The corresponding specified pressure in pump mode ranges at the high-pressure boundary between 80–220 kPa. The resulting area-weighted pressure at the low-pressure boundary is between 49–155 kPa in pump mode.

At the walls, a no-slip condition is applied. Wall viscous effects are taken into account using standard wall functions for all y^+ treatments since the average y^+ is around 8–30 for the different surfaces. The mentioned all y^+ treatments provide blending of the velocity profile from the viscous sublayer and the logarithmic layer in the buffer layer. The arbitrary mesh interface technique is used [37,38] to transfer information between the mesh regions.

4. Results and discussion

This section starts with an overview of all the evaluated cases in both pump and turbine modes. This is followed by an in-depth analysis of cavitation effects on the operating performance of the CRPT at different levels of cavitation.

Fig. 4 shows the normalised performance breakdown curves as a function of the Thoma number (Eq. (4)). At $\sigma \gtrsim 1.5$ a similar behaviour is noted in both modes. However, at smaller σ values a completely different behaviour is noted. In turbine mode, the performance parameters (Eqs. (1)–(3)) gradually decrease between $0.5 < \sigma < 1.0$, after which they stabilise. It is expected that the performance would drop further at σ less than 0.24. However, because of numerical instabilities, lower values could not be evaluated in the present study. In pump mode, the net head and power show a slight increase as σ falls below 1.5, which can indicate the inception of cavitation. It has been reported in the literature that a small increase in efficiency can be expected when the inception of cavitation occurs for pumps [39]. However, for the evaluated CRPT the efficiency is only decreasing, also when the head and power are increasing. This is explained by that the power increases more than the net head. As σ decreases below 1.2, the head and power rapidly decrease. Furthermore in pump mode, σ is decreasing from the largest value, reaching the smallest value of 0.94. However at this value, σ is increasing while the performance is reducing. The reason for this behaviour in pump mode lies in the definition of the Thoma number in Eq. (4). In the current study, the only variables that are changing in the Thoma number are the net head (H) of the CRPT and the static pressure on the low-pressure boundary of the computational domain (p_{LP}). The net head produced in pump mode is reducing faster than the static pressure on the low-pressure side as the head drops below 12% at $\sigma = 0.94$.

To better understand the operating performance of the CRPT, the performance breakdown curves are shown as a function of the pressure at the low-pressure boundary in Fig. 5. The turbine mode curves are essentially identical to those presented in Fig. 4. The pump mode curves on the other hand demonstrate a different appearance compared to when plotted as a function of σ. As expected the performance is decreasing with reduced inlet pressure at the lower inlet pressures. The main reason for the behaviour in turbine mode is that the denominator of the σ equation, representing the head, remains relatively stable while the numerator, representing the low-pressure value, significantly decreases. As a result, σ also decreases. However, in pump mode, the pump head undergoes a significant reduction, causing σ to eventually increase at a certain point as $p_{LP} < 64$ kPa.

Figs. 4 and 5 suggest that reducing the σ number results in a significant performance drop in pump mode, contrasting with the more stable behaviour of the machine in turbine mode. Thus, it can be concluded that the pump mode operation is more sensitive to cavitating conditions. The pump performance is practically constant for $\sigma > 1.5$. However, already at a $\sigma = 1.2$ the efficiency has dropped by 2.3% and continues to drop with decreasing inlet pressure. Fei et al. [40] indicated that for a conventional rotor-stator axial flow pump, a σ larger than 1.9 ensures unaffected performance, and that at σ less than 1.3 the performance drops drastically. The turbine mode operation of the CRPT is almost unchanged down to $\sigma = 1.0$. This can be compared to a bulb turbine, where Feng et al. [41] reported that the inception of cavitation occurs at a σ of 2.0, and that critical cavitation is developed at a σ of 1.2. Between $0.5 < \sigma < 1.0$ the head and efficiency drops by roughly 7% and severe cavitation is expected to develop somewhere between those values. The conventionally used 3% head drop [42] occurs at a σ of 1.0 in pump mode (neglecting the lower head values where σ is not unambiguous) and at 0.6 in turbine mode. The 3% head drop happens close to the points marked with B_P and B_T, which is why these operating conditions are later selected for a detailed investigation. To evaluate the occurrence of cavitation, the liquid volume fraction can be assessed.
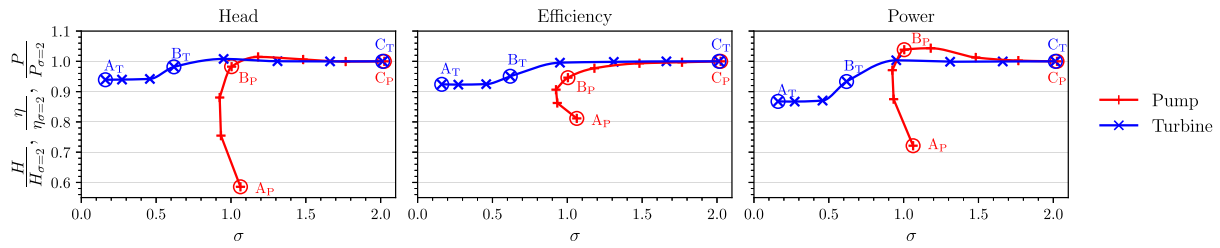
Fig. 4. Performance breakdown curves as a function of σ. Markers (+ and ×) represent CFD simulations and circles highlight cases selected for detailed analysis.
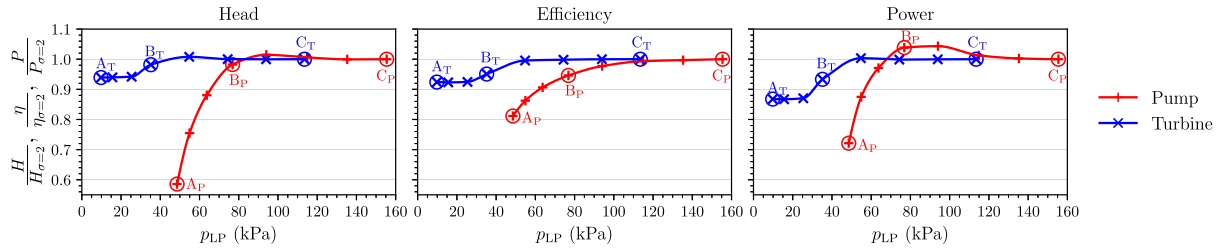

Fig. 5. Performance breakdown curves as a function of the static pressure at the low-pressure boundary in the computational domain p_{LP}. Markers (+ and ×) represent CFD simulations and circles highlight cases selected for detailed analysis.

Fig. 6 shows iso-surfaces of the liquid volume fraction (α_l) to visualise the cavitating regions close to the runners in turbine mode. It is seen that the cavitation primarily occurs on the downstream Runner 1 which is placed on the low-pressure side. As expected, the cavitating volume is larger at the smaller σ values. For the four cases on the top row, the suction side of the Runner 1 blades is almost completely covered by attached cavitation. Furthermore, tip leakage cavitation by the runner tips and the shroud is apparent. The tip leakage cavitation is caused by the pressure difference between the suction and pressure sides of the runner blades as explained by Laborde et al. [43]. A smaller amount of cavitation is visible by the leading edges of the upstream Runner 2. The similar appearance of the cavitating regions in Figs. 6(a)–6(d) explain the stable behaviour demonstrated by the performance curves at the lower σ. For the cases on the bottom row, the cavitating region is smaller and reduces by increasing the Thoma number. At $\sigma = 0.97$ (Fig. 6(e)), a large part of the cavitation on Runner 1 has vanished. At the largest evaluated σ (Fig. 6(g)) only a small amount of cavitation is noted at the suction side of the leading edge on one of the blades of the downstream Runner 1.

Similar iso-surfaces for the pump mode cases are shown in Fig. 15. The cavitating volume is, as anticipated, largest at the smallest p_{LP} (shown in Fig. 7(a)). Runner 1, which is located on the low-pressure side, is as in turbine mode more susceptible to cavitation. At this operating condition, the entire suction side of the upstream Runner 1 blades is covered by an attached cavitating region. On the downstream Runner 2, a smaller amount of cavitation is present by the leading edges. On both runners, cavitating tip leakage vortices are apparent. By evaluating the cases in Figs. 7(b)–7(d), the tip leakage cavitation is still noticeable. However, the cavitating region on Runner 1 is reduced at the trailing edges. From Fig. 7(d) to 7(e), the Runner 1 cavitating region is drastically reduced. By further increasing the inlet pressure, the cavitation diminishes and the tip leakage cavitation is no longer present, especially on the downstream Runner 2. For the cases with the highest inlet pressures, (Figs. 7(g)–7(h)), not much difference is noted and only a small amount of cavitation is noticeable at the leading edges of Runner 1. The notable increase in the cavitating volume by reducing p_{LP} explains the decrease in performance shown in Figs. 4 and 5. To have a nearly non-cavitating operation in pump mode, the Thoma number should be above 1.50, where only a smaller amount of attached cavitation is present at the leading edges of the runners.

The Thoma numbers in pump and turbine modes, which ensure close to unaffected performance, can be used to estimate an appropriate

submersion depth of the CRPT. Since the smallest Thoma number is larger in pump mode, the pump mode operation dictates the overall powerplant Thoma number. In the present study, the submersion ($h_{\min}$) of the machine should at least be 1.6 m, as given by

$$h_{\min} = \sigma_{\min} H - \frac{8 Q^2}{g \pi^2 D_{\mathrm{LP}}^4} + \frac{p_v - p_{\mathrm{atm}}}{\rho g}.$$

Here $\sigma_{\min}$ is the smallest allowed Thoma number (1.5 since pump mode is more severe than turbine mode), H is the pump net head (7.9 m in the present study), Q is the flow rate, g is the gravitational acceleration, D_{LP} is the diameter of low-pressure boundary, p_v is the vapour pressure, p_{atm} is the atmospheric pressure, and ρ is the fluid density.

Three operating conditions in each mode are chosen for an in-depth analysis of the reasons and mechanisms of the cavitation performance. The three cases are labelled A, B and C. Case A is experiencing the operating condition with a high level of cavitation (lowest p_{LP}), and C represents a low-cavitating regime (highest p_{LP}). To differentiate between the turbine and pump modes, the subscripts T and P are used for the corresponding mode. The cases are indicated by circles in Figs. 4 and 5.

4.1. Turbine mode detailed study

Fig. 8 shows instantaneous snapshots of the blade pressure distribution at the mid-span of a blade for each runner in turbine mode. Case A_T, which is experiencing the most cavitation, has the least favourable pressure distributions. This is because the entire suction side, and part of the pressure side, close to the trailing edge, of Runner 1 are at the vapour pressure level. Also, close to the leading edge of Runner 2 the pressure is at the vapour pressure. The sections of the blades experiencing the vapour pressure level align with the regions indicating cavitating regions in Fig. 6. Case B_T is indicating a similar appearance as A_T. However for B_T a smaller part of the Runner 2 suction side is at the vapour pressure, and the trailing edge of Runner 1 is slightly above the vapour pressure. At operating condition C_T, the blade pressure distribution is completely above the vapour pressure, which explains why C_T has the higher efficiency. This is because cavitation disrupts the ideal flow guidance by the blades, preventing them from performing as designed.

The effects of cavitation on the flow guidance by the runner blades are further assessed. Fig. 9 shows contours of the magnitude of the relative velocity and the corresponding surface streamlines on a cylindrical
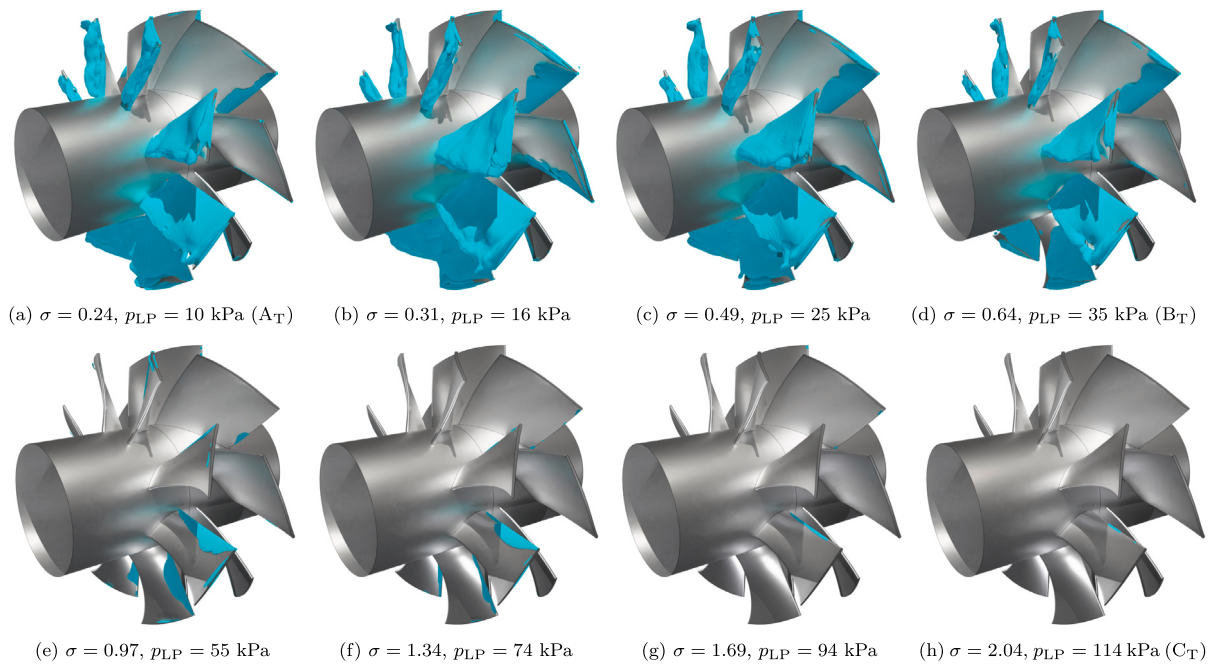
(a) $\sigma = 0.24$, $p_{\mathrm{LP}} = 10$ kPa (A$_\mathrm{T}$)   (b) $\sigma = 0.31$, $p_{\mathrm{LP}} = 16$ kPa   (c) $\sigma = 0.49$, $p_{\mathrm{LP}} = 25$ kPa   (d) $\sigma = 0.64$, $p_{\mathrm{LP}} = 35$ kPa (B$_\mathrm{T}$)

(e) $\sigma = 0.97$, $p_{\mathrm{LP}} = 55$ kPa   (f) $\sigma = 1.34$, $p_{\mathrm{LP}} = 74$ kPa   (g) $\sigma = 1.69$, $p_{\mathrm{LP}} = 94$ kPa   (h) $\sigma = 2.04$, $p_{\mathrm{LP}} = 114$ kPa (C$_\mathrm{T}$)

Fig. 6. Iso-surface of liquid volume fraction, $\alpha_\mathrm{l} = 0.9$, in turbine mode. The flow is from right to left, Runner 1 is downstream and Runner 2 is upstream.

(a) $\sigma = 1.09$, $p_{\mathrm{LP}} = 49$ kPa (A$_\mathrm{P}$)   (b) $\sigma = 0.95$, $p_{\mathrm{LP}} = 55$ kPa   (c) $\sigma = 0.94$, $p_{\mathrm{LP}} = 64$ kPa   (d) $\sigma = 1.02$, $p_{\mathrm{LP}} = 77$ kPa (B$_\mathrm{P}$)

(e) $\sigma = 1.20$, $p_{\mathrm{LP}} = 94$ kPa   (f) $\sigma = 1.50$, $p_{\mathrm{LP}} = 115$ kPa   (g) $\sigma = 1.78$, $p_{\mathrm{LP}} = 135$ kPa   (h) $\sigma = 2.04$, $p_{\mathrm{LP}} = 155$ kPa (C$_\mathrm{P}$)
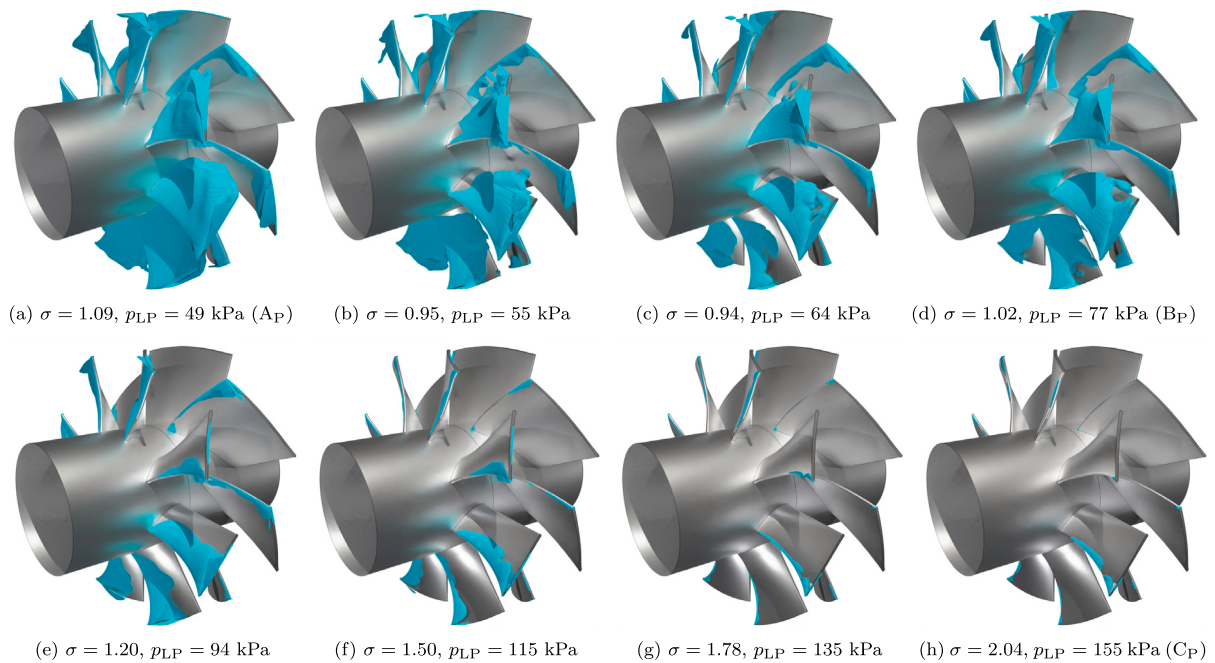
Fig. 7. Iso-surface of liquid volume fraction, $\alpha_\mathrm{l} = 0.9$, in pump mode. The flow is from left to right, Runner 1 is upstream and Runner 2 is downstream.
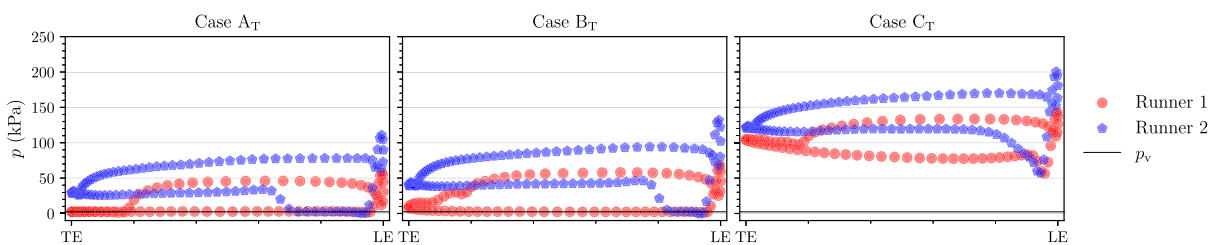

Fig. 8. Snapshots of blade mid-span pressure distribution in turbine mode. LE is the leading edge, TE is the trailing edge, and p_v is the vapour pressure.
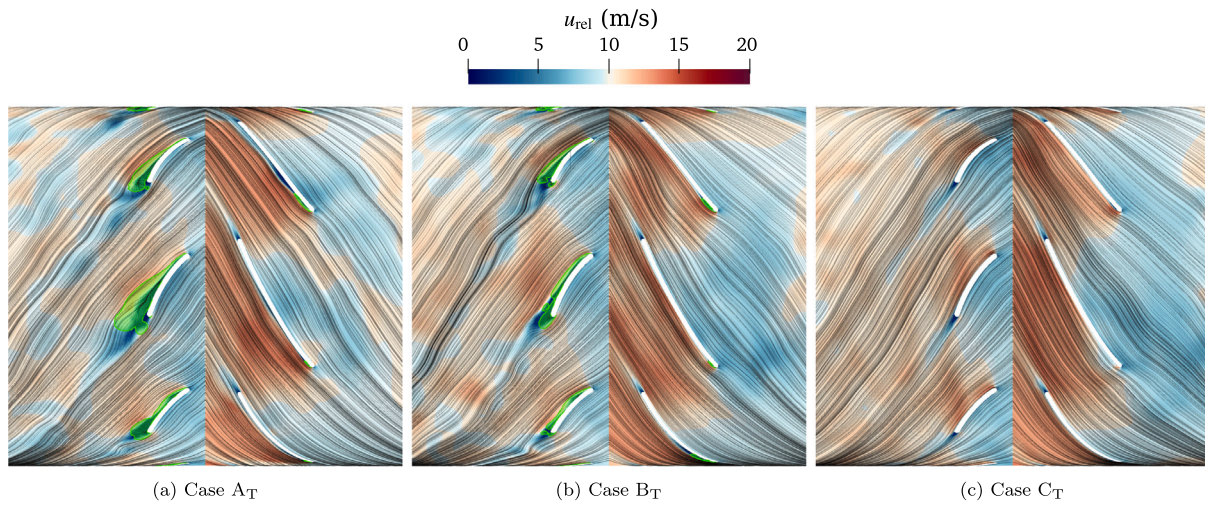
Fig. 9. Snapshots of contours of the magnitude of relative velocity and corresponding surface streamlines on a cylindrical cut plane at the mid-span in turbine mode. The shaded green areas show cavitating regions with $\alpha_l \leq 0.9$. The flow is from right to left, Runner 1 is downstream and Runner 2 is upstream.

cut plane at the mid-span in turbine mode. The upstream Runner 2 shows a consistent flow field for all cases, indicating effective flow guidance by the blades. However, at the downstream Runner 1 noticeable differences emerge. In both cases A_T and B_T, boundary layer flow separation begins at the leading edges of the blades' suction side. The separation grows into an unsteady wake downstream of the trailing edges. This is seen by the streamlines which do not follow the curvature of the blade surfaces. The Runner 1 wakes are largest for Case A_T since a larger part of the blades experiences cavitation, as illustrated by the shaded green areas. Hence, the separation region enlarges with the reduction of σ. The reason for this is that the cavitating region on the suction side of the Runner 1 blades prevents an attached flow. This is in contrast to Case C_T where the flow follows the blade shape and the Runner 1 wake is therefore almost negligible. The lack of the unsteady Runner 1 wake and aligned flow in C_T means lesser losses and thus a more stable operation as well as a higher efficiency.

To schematically visualise what the flow undergoes through the runners, Fig. 10 shows velocity triangles in turbine mode. They are given by temporally and spatially averaging the CFD results at planes located upstream, between and downstream the runners. The upstream Runner 2 velocity triangles are practically identical for the three cases. This means that the incoming flow for the downstream Runner 1 is the same and that the main differences in operating performance originate from that runner. Downstream of Runner 1, Case A_T shows the largest absolute tangential velocity whereas C_T the smallest. Furthermore, it is noticeable that B_T has a marginally larger tangential velocity after the runners than in C_T. A larger negative absolute tangential velocity downstream of Runner 1 means that the runner has not been able to de-swirl the flow properly leaving the upstream Runner 2. Thus, with more cavitation the flow separation increases, leading to a smaller change in tangential flow direction over Runner 1. According to the Euler turbine equation, a smaller change in tangential flow direction over a runner leads to a decrease in power. Therefore, by applying the Euler turbine equation between C_T and A_T,

$$\left[1 - \frac{\Delta u_{\theta,C,R1}(\omega_{R1}/\omega_{R2}) + \Delta u_{\theta,C,R2}}{\Delta u_{\theta,A,R1}(\omega_{R1}/\omega_{R2}) + \Delta u_{\theta,A,R2}} \right] 100 = 11.4\%, \tag{12}$$

it is shown that the seemingly small differences in tangential velocity between the cases are responsible for most of the decrease in power. As a reference, the total decrease in power in Figs. 4 and 5 between C_T and A_T is 13.2%.

Fig. 11 shows the power spectral density (PSD) obtained from a fast Fourier transform (FFT) of the fluctuating component of the pressure at probe $P3_{pos}$ in turbine mode. The probe is located at the shroud between the runners, as shown in Fig. 2. The frequency is normalised by

the blade passing frequency of the upstream Runner 2, $f_{R2} = 73.9$ Hz. In turbine mode this corresponds to that $\hat{f}_T = f/f_{R2}$. For all cases, the expected blade passing frequency of each runner, as well as linear combinations of the blade passing frequencies and various harmonics, are indicated by peaks. For instance, the blade passing frequency of Runner 2 is shown at multiples of 1. The blade passing frequency of Runner 1 (f_{R1}) is indicated at multiples of 1.521. Linear combinations of the blade passing frequencies 2.521 ($f_{R1} + f_{R2}$), as well as 3.521 ($f_{R1} + 2f_{R2}$) are also indicating peaks. An additional non-trivial peak at $0.396\hat{f}_T = 29.4$ Hz is observed for all the cases. Furthermore, Case B_T demonstrate a peak at $0.062\hat{f}_T = 4.6$ Hz, and at its second harmonic frequency of $0.125\hat{f}_T = 9.2$ Hz, which are not seen in the other cases. The 0.062 frequency, and its second harmonic, are connected to the cavitation phenomenon as it is not present in the other scenarios. All these non-trivial peaks are examined and explained in the subsequent paragraphs.

A modal analysis can help discover the origin of the non-trivial frequencies demonstrated in Fig. 11. The dynamic mode decomposition (DMD) [44] method is a widely used modal analysis technique, utilised to analyse the time snapshots of a flow field and extract physical flow patterns. Unlike proper orthogonal decomposition, which produces spatially orthogonal modes, DMD focuses on temporal orthogonality, meaning that each mode oscillates with an isolated frequency that can be connected to a distinct physical phenomenon. Therefore, the eigenmodes of the DMD algorithm offer a detailed picture of the flow field's coherent structures and can be used to uncover the origin of unknown frequency excitations.

The modal analysis is performed on Case B_T using the sparsity-promoting variation of the DMD algorithm (SPDMD) [45] to extract a subset of the most influential DMD modes. The chosen case demonstrates all the observed non-trivial frequencies that need to be investigated.

The pressure distribution is recorded on the midplane at a DMD sampling interval of 5×10^{-3} s, and the total considered sampling time is 1.5 s. These two parameters are chosen based on the targeted frequencies. The sampling interval is fine enough to effectively capture the highest frequency of interest while the total sampling time is chosen so that it contains several repetitions of the coherent structures with the lowest frequency of interest.

The real part of the first 9 SPDMD eigenmodes of the midplane is shown in Fig. 12. Mode 1 (Fig. 12(a)) is stationary and represents the time-averaged flow field. Modes 3, 5, and likely 13, (Figs. 12(b), 12(c), and 12(g)) represent the patterns causing the pressure pulsation peak close to 0.062. These pulsations are connected to the wake region
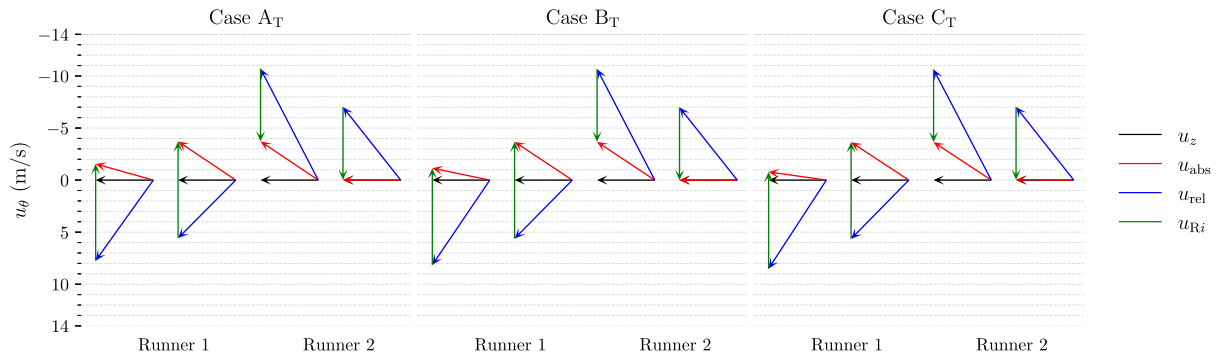
Fig. 10. Temporally and spatially averaged velocity triangles in turbine mode from planes located upstream, between and downstream of the runners.
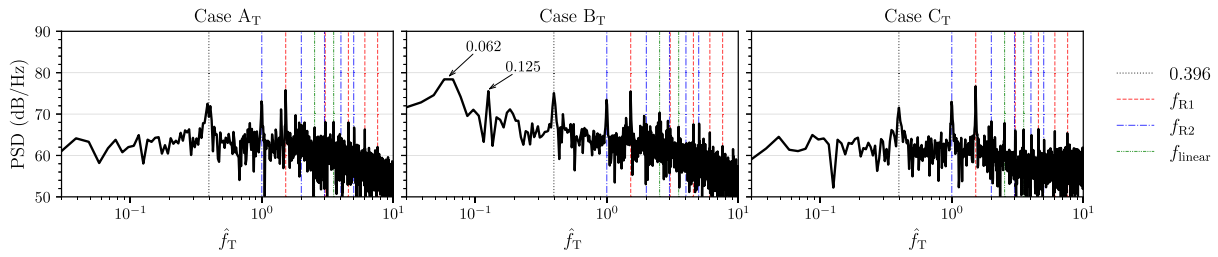

Fig. 11. PSD of pressure at probe P3$_{pos}$ (see Fig. 2) as a function of frequency normalised by the Runner 2 blade passing frequency in turbine mode. The f_{R1} and f_{R2} lines show the main and harmonic frequencies for Runner 1 and Runner 2, respectively. The f_{linear} lines indicate linear combinations of f_{R1} and f_{R2}.

(a) Mode 1, $\hat{f}_T = 0.000$ (b) Mode 3, $\hat{f}_T = 0.062$ (c) Mode 5, $\hat{f}_T = 0.050$

(d) Mode 7, $\hat{f}_T = 0.121$ (e) Mode 9, $\hat{f}_T = 0.415$ (f) Mode 11, $\hat{f}_T = 0.396$

(g) Mode 13, $\hat{f}_T = 0.074$ (h) Mode 15, $\hat{f}_T = 0.113$ (i) Mode 17, $\hat{f}_T = 0.384$
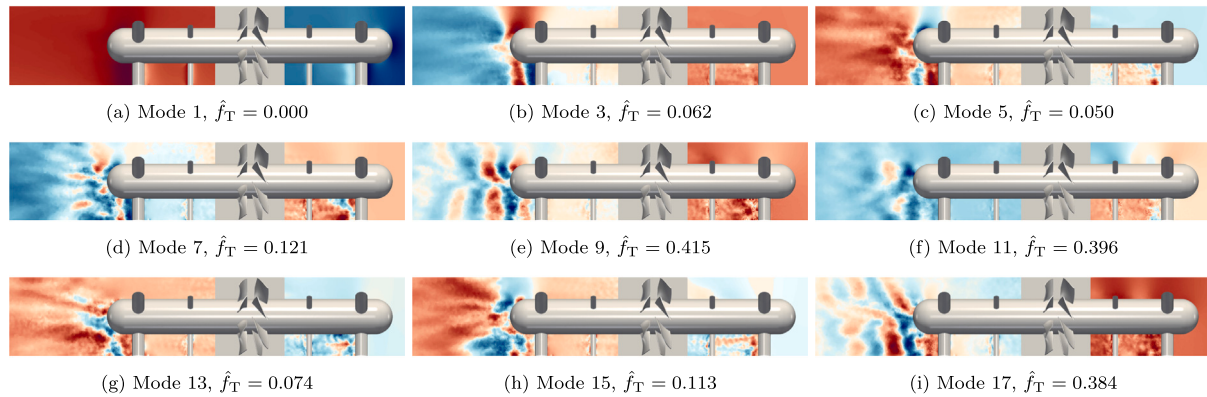
Fig. 12. Real part of the first 9 SPDMD modes at the vertical cut plane with their corresponding dimensionless frequencies in Case B$_T$. Note flow is from right to left, and mode 1 has a negative SPDMD coefficient.

formed by the set of larger support struts located on the downstream side of the machine. Mode 7 (Fig. 12(d)) has roughly twice the frequency of Mode 3, and the frequency of Mode 15 (Fig. 12(h)) is about double the frequency of Mode 5. It is therefore assumed that modes 7 and 15 represent the second harmonic of modes 3 and 5, respectively. Modes 9, 11, and 17 (Figs. 12(e), 12(f), and 12(i)) have frequencies close to the 0.395 peak. That peak is apparent in all the cases and the pulsations are predominately caused by the combined vortex shedding from the support struts and volume expansion at the spherical part of the mounting arrangement. This phenomenon is visually represented by the observed repairing pattern downstream of the mounting arrangement in Fig. 12(e).

Arabnejad et al. [20] explained that vapour volume fluctuations can excite pressure fluctuations because of the changing size of the vapour cloud. Fig. 13 shows the PSD of the vapour volume fluctuations for the turbine mode cases. In cases A$_T$ and C$_T$ no clear peaks are observed. However, in Case B$_T$ a strong peak arises at 0.068 and a smaller peak at double that normalised frequency at 0.136. The normalised vapour volume frequency of 0.068 appears at a frequency which is around 10% higher than the observed 0.062 pressure frequency at P3$_{pos}$. Later on in

Section 4.2 it is found that also in pump mode the vapour volume fluctuations have associated frequencies which are at a frequency that is about 10% higher than the corresponding excited pressure fluctuations frequency. An explanation of why the vapour volume fluctuation has a frequency slightly higher than the corresponding excited pressure oscillation is because the vapour volume region must be smaller than the equivalent wake region causing the pressure pulsation. The smaller region consequently explains the higher frequency detected for the vapour volume fluctuations compared to the pressure fluctuations.

The excitation of the normalised pressure pulsation frequency at 0.062 is shown to originate from the presence of the larger downstream support struts and is related to the cavitating flow. Fig. 14 shows isosurfaces of the liquid volume fraction close to the larger downstream support struts. In this figure, Case C$_T$ is neglected since there is no cavitation present by the downstream support struts. In Case A$_T$, almost the entire region downstream of the support struts is consistently occupied by a cavitating flow with relatively stable characteristics. In contrast, Case B$_T$ indicates an oscillatory cavitating pattern characterised by the formation and detachment of vortices from the struts in the form
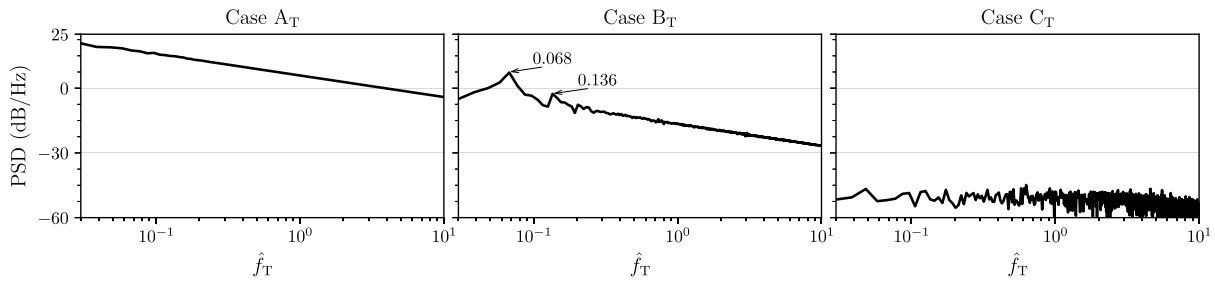
Fig. 13. PSD of fluctuating component of vapour volume as a function of normalised frequency in turbine mode.
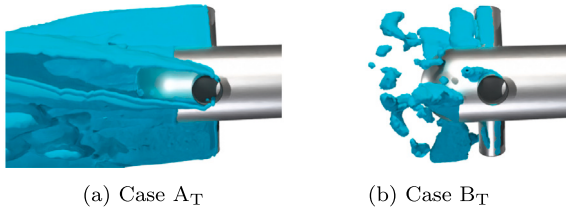

(a) Case A_T (b) Case B_T

Fig. 14. Iso-surface of liquid volume fraction, $\alpha_l = 0.9$, close to the large downstream support struts in turbine mode. The flow is from right to left.

of vortex shedding phenomena. Hence the 0.062 pressure oscillation frequency is arguably connected to the change in vapour volume.

4.2. Pump mode detailed study

Fig. 15 shows the blade pressure distribution at the mid-span on a blade for both runners in pump mode. Similar to most of the turbine mode cases, a desired pressure distribution on Runner 1 cannot be maintained in pump mode due to the presence of cavitation. Note that the CRPT operates at a larger net head in pump mode, which explains the larger difference in pressure between the suction and pressure sides of the blades in pump mode compared to in turbine mode. Additionally, the flow direction is changed, which is why the leading edge is placed to the left in Fig. 15. In Case A_P, the pressure distribution at the entire suction side of the Runner 1 blade is close to the vapour pressure. This allows for the development of cavitation on the entire suction side of the Runner 1 blades, which is seen in Fig. 7(a). Furthermore in Case A_P, the Runner 1 pressure side has a region, at around 17% from the leading edge, where cavitation can develop since the pressure is at the vapour pressure level. Increasing the inlet pressure, and thus reducing the amount of cavitation, in cases B_P and C_P, results in a more reasonable pressure distribution which is closer to the design conditions. However also in Case B_P, the Runner 1 suction side is close to the vapour pressure level, which may interfere with the ideal flow guidance. Even at C_P, the leading edge pressure is close to the vapour pressure which indicates cavitation. This is confirmed by the limited amount of cavitation observed at the Runner 1 leading edges in Fig. 7(h).

To visualise the effects caused by cavitation on the flow guidance by the blades, Fig. 16 shows contours of the magnitude of the relative velocity and the corresponding surface streamlines on a cylindrical cut plane at the mid-span in pump mode. For Case A_P, large separated regions are developed on the suction side of the Runner 1 blades and detach downstream of the runner. The detached Runner 1 wake causes reverse flow between the runners, which deteriorates the performance. Additionally, separated regions are detected close to the Runner 1 leading edges on the pressure side. The separation regions on the blades' pressure side occur at the location where the pressure is close to the vapour pressure, see Fig. 15. In Case B_P the flow detachment is smaller than in A_P. However, an unsteady wake is also developed

downstream of Runner 1 in B_P. For Case C_P the flow follows the Runner 1 blade shape more closely compared to the other cases. The flow at Runner 2 demonstrates a more aligned flow for all cases compared to the Runner 1 flow indicating that the flow is adequately guided by the blades regardless of the Thoma number. This is explained by the fact that cavitation is predominantly present at Runner 1 as illustrated by the shaded green areas.

By evaluating the velocity triangles shown in Fig. 17 a graphical representation of how the flow changes over the runners with respect to cavitation is given. In Case A_P the relative velocity leaving Runner 1 is larger than for the other cases. This means that in A_P less angular momentum is added to the flow over Runner 1. The result of this is a lower power and more importantly that the relative flow angle entering Runner 2 is smaller. As an effect of this, the absolute flow angle leaving Runner 2 is larger for Case A_P than for the other cases. Ideally, the flow leaving Runner 2 should be purely axial, any remaining swirling flow is simply an energy loss which in turn reduces the efficiency of the machine. Comparing cases B_P and C_P, it is found that the relative flow leaving Runner 1 is larger in B_P. Furthermore, the absolute flow leaving Runner 2 has a marginally larger flow angle in Case B_P than in C_P. The smaller relative flow angle leaving Runner 1 together with the larger absolute flow angle leaving Runner 2 partly explains the higher power and lower efficiency noted for B_P than for C_P in Figs. 4 and 5. Applying Eq. (12) to compare cases C_P and A_P, the reduction in power is about 10% by only evaluating the velocity triangles. The main performance loss is thus explained by the cavitating region, which causes flow separation on the Runner 1 blades suction side, as shown in Fig. 16.

The effect of cavitation on the pressure oscillations is investigated through the PSDs of fluctuating pressure at different cavitating conditions in Fig. 18. The PSD is derived from the fluctuating component of the pressure at probe $P3_{pos}$ (see Fig. 2) and is presented as a function of the normalised frequency $\hat{f}_P$. The frequency $\hat{f}_P$ is normalised with the blade passing frequency of the upstream Runner 1, $f_{R1} = 150.6$ Hz.

Similar to the turbine mode, the expected blade passing frequency of each runner is indicated for all the cases, as well as linear combinations and harmonics. Traces of the blade passing frequency of Runner 1 is indicated as multiples of 1, whereas the Runner 2 blade passing frequency (f_{R2}) is shown at multiples of 0.658. Consequently the first linear combination ($f_{R1} + f_{R2}$) is indicated at 1.658.

The non-trivial peak at 0.195 is distinguishable in all cases, however most noticeable in Case C_P. The frequency of this peak is $0.195\hat{f}_P = 29.4$ Hz. This is the same frequency as the turbine mode pressure oscillation peak at $0.396\hat{f}_T$, shown in Fig. 11. Therefore, it is arguably assumed that this peak in pump mode originates from the same physical phenomena as the turbine mode peak, which is caused by the combined vortex shedding of the support struts. This is furthermore confirmed later in the text when discussing the results from an SPDMD analysis, see Fig. 21. Additional non-trivial pressure oscillation peaks in Fig. 18 are present for cases A_P and B_P. In Case A_P there is a peak at $0.049\hat{f}_P = 7.4$ Hz, whereas in B_P a peak is at $0.155\hat{f}_P = 23.3$ Hz. These non-trivial frequencies are investigated in the subsequent paragraphs.
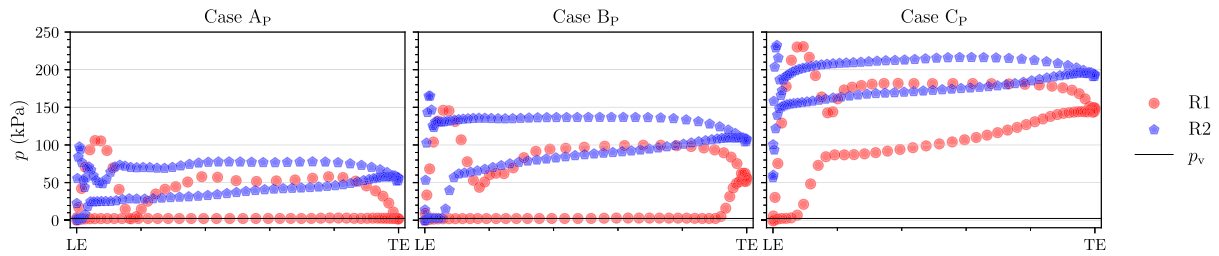
Fig. 15. Snapshots of blade mid-span pressure distribution in pump mode. LE is the leading edge, TE is the trailing edge, and p_v is the vapour pressure.
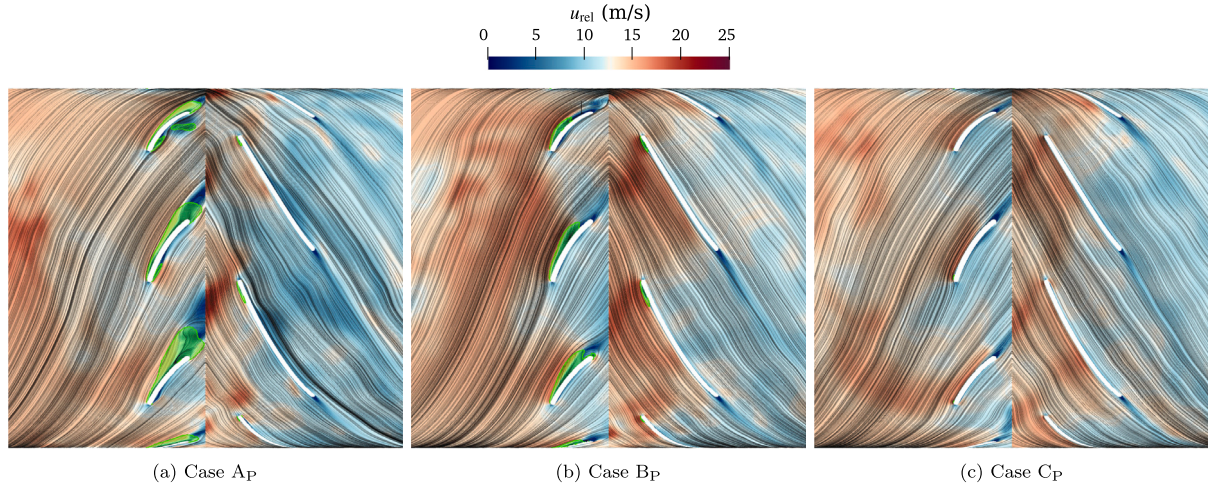

Fig. 16. Snapshots of contours of the magnitude of relative velocity and corresponding surface streamlines on a cylindrical cut plane at the mid-span in pump mode. The shaded green areas show cavitating regions with $\alpha_l \leq 0.9$. The flow is from left to right, Runner 1 is upstream and Runner 2 is downstream.
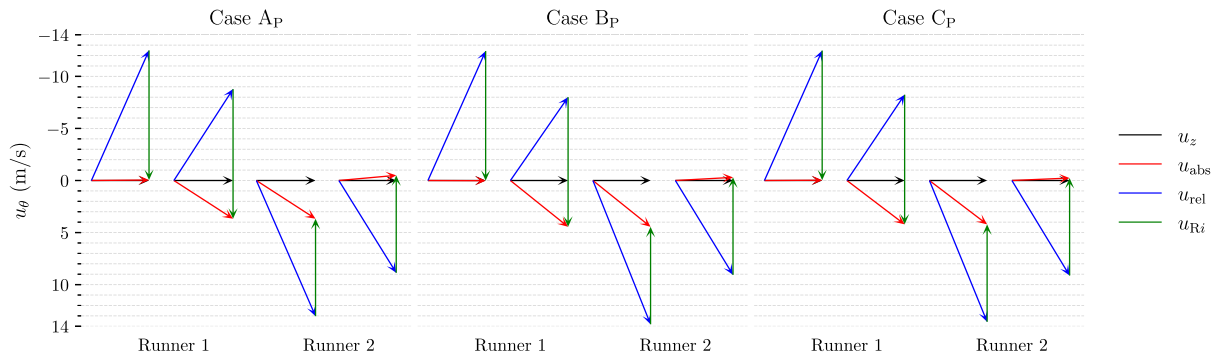

Fig. 17. Temporally and spatially averaged velocity triangles in pump mode from planes located upstream, between and downstream of the runners.
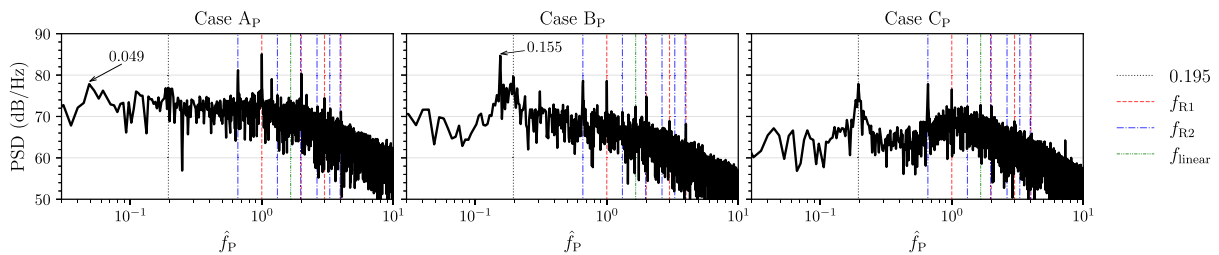

Fig. 18. PSD of pressure at probe P3$_{pos}$ (see Fig. 2) as a function of frequency normalised by the Runner 1 blade passing frequency in pump mode. The f_{R1} and f_{R2} lines show the main and harmonic frequencies for Runner 1 and Runner 2, respectively. The f_{linear} lines indicate linear combinations of f_{R1} and f_{R2}.

To further discuss the non-trivial frequencies, the PSD of the fluctuating component of the vapour volume is shown in Fig. 19. The A_P case has a peak at 0.053, whereas a peak is at 0.177 in Case B_P. An additional peak at 0.221 is distinguishable in B_P and C_P. All

these vapour volume peaks are at a frequency that is between 8%–14% higher than a corresponding pressure oscillation peak noted at the pressure probe P3$_{pos}$. The 0.053 vapour volume peak has the corresponding pressure peak at 0.049 in A_P. Similarly, the 0.177 vapour
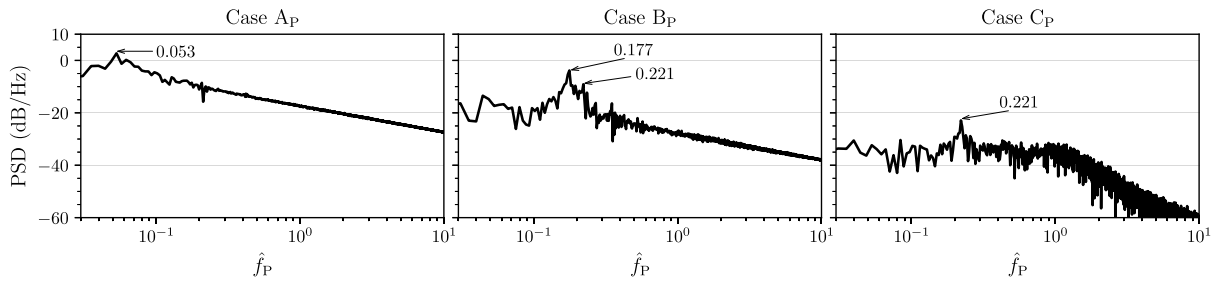
Fig. 19. PSD of fluctuating component of vapour volume as a function of normalised frequency in pump mode.
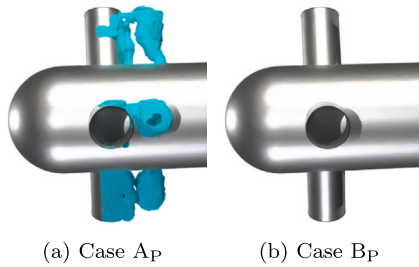

(a) Case A_P (b) Case B_P

Fig. 20. Iso-surface of liquid volume fraction, $\alpha_l = 0.9$, close to the larger upstream support struts in pump mode. The flow is from left to right.

volume peak is linked to the 0.155 pressure peak in B_P and the 0.221 vapour peak is correlated to the 0.195 peak. As mentioned previously, in turbine mode Case B_T, the pressure oscillation peak at $0.062\hat{f}_T$ has a corresponding vapour volume peak at a frequency which is around 10% higher, at $0.068\hat{f}_T$.

The 0.053 volume fraction, or 0.049 pressure, peak for Case A_P is assumed to be because of the set of larger support struts. Fig. 20 shows iso-surfaces of the liquid volume fraction close to the upstream larger support struts for cases A_P and B_P. In Case A_P an unsteady cavitating region is apparent downstream of the struts, whereas in B_P no sign of cavitation by the larger support struts is visible. Therefore, it is likely that the vapour volume fraction peak is because of the larger support struts. The 0.053 peak in Case A_P is in that case caused by a similar phenomenon as the vapour volume peak at $0.068\hat{f}_T$ found in turbine mode Case B_T. Note that Case C_P is excluded in Fig. 20 since no sign of cavitation by the larger support struts is observable.

To find a plausible explanation for the non-trivial pressure oscillation peak at the normalised frequency 0.155 in Case B_P an SPDMD analysis is carried out. Fig. 21 shows the real part of the first 9 SPDMD eigenmodes of the vertical cut plane in Case B_P. The time-average flow field is represented by Mode 1 (Fig. 21(a)). The pressure oscillation peak at 0.155 is predominately explained by modes 3 (Fig. 21(b)) and 7 (Fig. 21(d)), and potentially also by modes 9 (Fig. 21(e)) and 17 (Fig. 21(i)). These modes are mostly active between the two sets of support struts on the low-pressure side (left) of the CRPT. However, also some large-scale motions are noted downstream of the CRPT which seems to be connected to the volume expansion as the mounting arrangement ends. Modes 5 (Fig. 21(c)), 13 (Fig. 21(g)), and 15 (Fig. 21(h)) represent the physical phenomena which are causing the pressure peak at 0.195 seen in all the pump mode cases. Also, these modes are active around the low-pressure support struts. On the other hand, these modes show a stronger spatially reappearing pattern downstream of the CRPT, after the mounting arrangement. This is especially clear in Mode 15 and indicates that this mode is because of the vortex from the support struts as the volume expands by the spherical part of the mounting arrangement.

5. Conclusions

Cavitating flow simulations were carried out on a model scale contra-rotating pump-turbine to determine how the presence of cavitating flow affects the machine's operating capability in turbine and pump modes. The operating conditions were based on specifying an inlet flow rate of 0.27 m^3/s and varying the outlet pressure. The largest evaluated outlet pressure was set to match the Thoma number (σ) in both modes to roughly 2.0. In total 16 cavitating flow simulations were carried out, eight in turbine mode and eight in pump mode. Three cases in each mode were selected for a more detailed analysis to uncover how and why the CRPT's operating performance was affected by cavitation.

A comparison between the turbine and pump modes revealed that the pump mode was more sensitive to cavitation and experienced a larger performance drop. In turbine mode, the 3% head drop occurred at a Thoma number of 0.6, whereas in pump mode it happened at 1.0. It was in both modes shown that already at the 3% head drop, the suction side of the Runner 1 (the runner facing the lower reservoir) blades were mostly covered by cavitating flow. To have a close to cavitating-free operating condition and unaffected performance, the Thoma number should be above 1.0 in turbine mode and at least above 1.5 in pump mode. Additionally in pump mode, the conventional Thoma number was not reliable at inlet pressures less than 64 kPa ($\sigma_{min} = 0.94$) because of that the net head that the machine was able to produce, was reducing faster than the pressure on the low-pressure side of the computational domain. This resulted in σ starting to increase with reducing machine performance at the lower inlet pressures, below 64 kPa.

In both modes, Runner 1 was exposed to the largest effects caused by cavitation. This is explained by that Runner 1 is facing the lower reservoir and thus operates at a lower pressure than Runner 2. It was found that when cavitation was present by the runner blades, the flow could not be properly guided by the blades. This resulted in flow separation on the Runner 1 blades suction side, which in turn grew into a wake region downstream of the runner. The Runner 1 flow separation and wakes are some of the main reasons why there is a loss in operating performance when the CRPT experiences cavitation.

The findings of this study are important for understanding how cavitation affects the CRPT in various operations. The results can thus be vital when planning potential future low-head pumped hydro storage facilities since the contra-rotating runner configuration is a promising design for low-head sites. For future studies, the Runner 1 blade shape could potentially benefit from an optimisation study to limit the risk of flow separation at the leading edges. Another design suggestion is to change the load distribution in pump mode, allowing a higher load on Runner 2 (facing the upper reservoir). Such a design could potentially reduce the risk of cavitation since the head and power produced by the low-pressure Runner 1 would in that case be decreased. However, a strong argument for using a CRPT is to avoid having guide vanes to generate/remove swirl before/after the runners. This makes it complex to change the load distribution too much in favour for one of the runners since the swirl velocity is a function of the runner loads. Additionally, optimising the design of the mounting arrangement and support struts could mitigate the issues of large vortex shedding. This
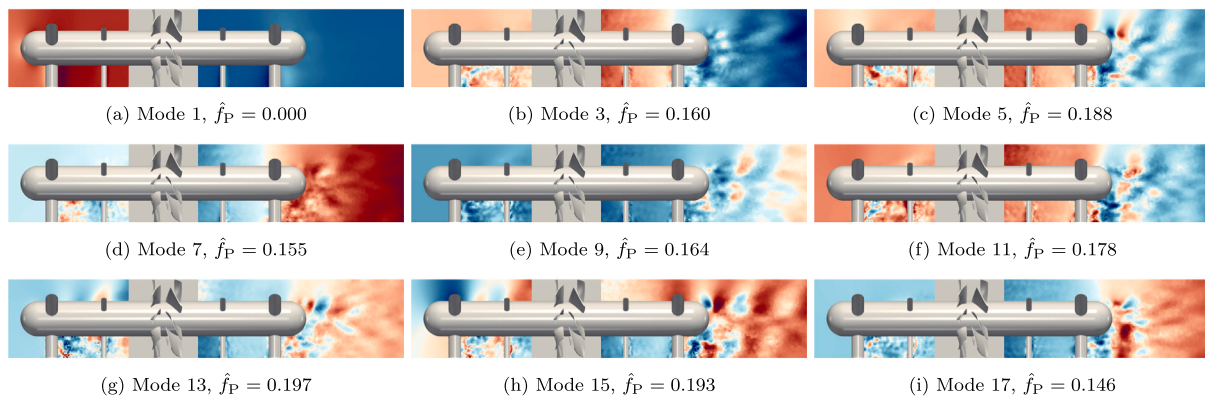
(a) Mode 1, $\hat{f}_{\mathrm{P}} = 0.000$

(b) Mode 3, $\hat{f}_{\mathrm{P}} = 0.160$

(c) Mode 5, $\hat{f}_{\mathrm{P}} = 0.188$

(d) Mode 7, $\hat{f}_{\mathrm{P}} = 0.155$

(e) Mode 9, $\hat{f}_{\mathrm{P}} = 0.164$

(f) Mode 11, $\hat{f}_{\mathrm{P}} = 0.178$

(g) Mode 13, $\hat{f}_{\mathrm{P}} = 0.197$

(h) Mode 15, $\hat{f}_{\mathrm{P}} = 0.193$

(i) Mode 17, $\hat{f}_{\mathrm{P}} = 0.146$

Fig. 21. Real part of the first 9 SPDMD modes of the vertical cut plane with their corresponding dimensionless frequencies in Case B_{P}. Note flow is from left to right, and mode 1 has a negative SPDMD coefficient.

is because this study has through a modal analysis using dynamic mode decomposition shown that the support struts are connected to some of the strongest pressure pulsations which also interact with the change in vapour volume.

CRediT authorship contribution statement

Jonathan Fahlbeck: Writing – review & editing, Writing – original draft, Visualization, Validation, Software, Project administration, Methodology, Investigation, Formal analysis, Conceptualization. **Håkan Nilsson:** Writing – review & editing, Supervision, Resources, Project administration, Funding acquisition, Conceptualization. **Mohammad Hossein Arabnejad:** Writing – review & editing, Methodology. **Saeed Salehi:** Writing – review & editing, Supervision, Software, Methodology, Formal analysis, Conceptualization.

Declaration of competing interest

The authors declare that they have no known competing financial interests or personal relationships that could have appeared to influence the work reported in this paper.

Acknowledgements

References

[1] H.E. Murdock, et al., Renewables 2021 - Global Status Report, Tech. Rep. 978-3-948393-03-8, France, 2021, p. 603, INIS-FR–21-0788.

[2] J.P. Hoffstaedt, et al., Low-head pumped hydro storage: A review of applicable technologies for design, grid integration, control and modelling, Renew. Sustain. Energy Rev. 158 (2022) 112119, http://dx.doi.org/10.1016/j.rser.2022.112119.

[3] ALPHEUS H2020, 2024, URL https://alpheus-h2020.eu/. Accessed on 16 January 2024.

[4] M. Qudaih, et al., The contribution of low-head pumped hydro storage to a successful energy transition, in: Proceedings of the Virtual 19th Wind Integration Workshop, 2020.

[5] R. Ansorena Ruiz, et al., Low-head pumped hydro storage: A review on civil structure designs, legal and environmental aspects to make its realization feasible in seawater, Renew. Sustain. Energy Rev. 160 (2022) 112281, http://dx.doi.org/10.1016/j.rser.2022.112281.

[6] A. Furukawa, T. Shigemitsu, S. Watanabe, Performance test and flow measurement of contra-rotating axial flow pump, J. Therm. Sci. 16 (1) (2007) 7–13, http://dx.doi.org/10.1007/s11630-007-0007-4.

[7] J. Fahlbeck, H.a. Nilsson, S. Salehi, Surrogate based optimisation of a pump mode startup sequence for a contra-rotating pump-turbine using a genetic algorithm and computational fluid dynamics, J. Energy Storage 62 (2023) 106902, http://dx.doi.org/10.1016/j.est.2023.106902.

[8] E.B. Prasasti, M. Aouad, M. Joseph, M. Zangeneh, K. Terheiden, Optimization of pumped hydro energy storage design and operation for offshore low-head application and grid stabilization, Renew. Sustain. Energy Rev. 191 (2024) 114122, http://dx.doi.org/10.1016/j.rser.2023.114122.

[9] E.B. Prasasti, M. Joseph, X. Miao, M. Zangeneh, K. Terheiden, Design of shaft- and rim-driven contra-rotating reversible pump-turbine to optimize novel low-head pumped hydro energy storages, Energy (2024) 132237, http://dx.doi.org/10.1016/j.energy.2024.132237.

[10] R. Tao, R. Xiao, F. Wang, W. Liu, Cavitation behavior study in the pump mode of a reversible pump-turbine, Renew. Energy 125 (2018) 655–667, http://dx.doi.org/10.1016/j.renene.2018.02.114.

[11] S.-J. Kim, H.-M. Yang, J. Park, J.-H. Kim, Investigation of internal flow characteristics by a Thoma number in the turbine mode of a Pump–Turbine model under high flow rate, Renew. Energy 199 (2022) 445–461, http://dx.doi.org/10.1016/j.renene.2022.08.157.

[12] L.L. Cao, S. Watanabe, T. Imanishi, S. Momosaki, A. Furukawa, On high efficiency operation of contra-rotating axial flow pump with rotational speed control toward effective energy saving, IOP Conf. Ser.: Earth Environ. Sci. 15 (4) (2012) 042027, http://dx.doi.org/10.1088/1755-1315/15/4/042027, Publisher: IOP Publishing.

[13] L. Cao, S. Watanabe, S. Momosaki, T. Imanishi, A. Furukawa, Low speed design of rear rotor in contra-rotating axial flow pump, Int. J. Fluid Mach. Syst. 6 (2) (2013) 105–112, http://dx.doi.org/10.5293/IJFMS.2013.6.2.105.

[14] T. Shigemitsu, A. Furukawa, S. Watanabe, K. Okuma, Air/water two-phase flow performance of contra-rotating axial flow pump and rotational speed control of rear rotor, in: ASME 2005 Fluids Engineering Division Summer Meeting, American Society of Mechanical Engineers Digital Collection, 2008, pp. 1069–1074, http://dx.doi.org/10.1115/FEDSM2005-77002.

[15] R. Hirschi, P. Dupont, F. Avellan, J.-N. Favre, J.-F. Guelich, E. Parkinson, Centrifugal pump performance drop due to leading edge cavitation: Numerical predictions compared with model tests, J. Fluids Eng. 120 (4) (1998) 705–711, http://dx.doi.org/10.1115/1.2820727.

[16] T. Lei, Z.B. Shan, C.S. Liang, W.Y. Chuan, W.B. Bin, Numerical simulation of unsteady cavitation flow in a centrifugal pump at off-design conditions, Proc. Inst. Mech. Eng. C 228 (11) (2014) 1994–2006, http://dx.doi.org/10.1177/0954406213514573.

[17] H. Ding, F.C. Visser, Y. Jiang, M. Furmanczyk, Demonstration and validation of a 3D CFD simulation tool predicting pump performance and cavitation for industrial applications, J. Fluids Eng. 133 (1) (2011) http://dx.doi.org/10.1115/1.4003196.

[18] M.M. Shamsuddeen, J. Park, Y.-S. Choi, J.-H. Kim, Unsteady multi-phase cavitation analysis on the effect of anti-cavity fin installed on a Kaplan turbine runner, Renew. Energy 162 (2020) 861–876, http://dx.doi.org/10.1016/j.renene.2020.08.100.

[19] M.H. Arabnejad, U. Svennberg, R.E. Bensow, Numerical assessment of cavitation erosion risk in a commercial water-jet pump, J. Fluids Eng. 144 (5) (2022) http://dx.doi.org/10.1115/1.4052634.

[20] M.H. Arabnejad, H.a. Nilsson, R.E. Bensow, Investigation of flow-induced instabilities in a francis turbine operating in non-cavitating and cavitating part-load conditions, Fluids 8 (2) (2023) 61, http://dx.doi.org/10.3390/fluids8020061.

[21] J.P. Hoffstaedt, R.A. Ruiz, D. Schürenkamp, A. Jarquin-Laguna, N. Goseberg, Experimental Setup and Methods for a Novel Low-Head Pumped Storage System, IET Digital Library, 2023, pp. 341–348, http://dx.doi.org/10.1049/icp.2023.1589.

[22] International Electrotechnical Commission, IEC 60193:1999, 1999, Hydraulic turbines, storage pumps and pump-turbines – Model acceptance tests.

[23] OpenCFD, OpenFOAM - The Open Source CFD Toolbox - User's Guide, Version v2112, OpenCFD Ltd, 2021.

[24] F. Menter, Y. Egorov, A scale adaptive simulation model using two-equation models, in: 43rd AIAA Aerospace Sciences Meeting and Exhibit, 2005, p. 1095, http://dx.doi.org/10.2514/6.2005-1095.

[25] F.R. Menter, Y. Egorov, The scale-adaptive simulation method for unsteady turbulent flow predictions. Part 1: Theory and model description, Flow Turbul. Combust. 85 (1) (2010) 113–138, http://dx.doi.org/10.1007/s10494-010-9264-5.

[26] C. Trivedi, Investigations of compressible turbulent flow in a high-head Francis turbine, J. Fluids Eng. 140 (1) (2017) http://dx.doi.org/10.1115/1.4037500.

[27] J. Unterluggauer, V. Sulzgruber, E. Doujak, C. Bauer, Experimental and numerical study of a prototype Francis turbine startup, Renew. Energy 157 (2020) 1212–1221, http://dx.doi.org/10.1016/j.renene.2020.04.156.

[28] J.-W. Suh, H.-M. Yang, J.-H. Kim, W.-G. Joo, J. Park, Y.-S. Choi, Unstable S-shaped characteristics of a pump-turbine unit in a lab-scale model, Renew. Energy (2021) http://dx.doi.org/10.1016/j.renene.2021.03.013.

[29] H. Weller, Controlling the computational modes of the arbitrarily structured C grid, Mon. Weather Rev. 140 (10) (2012) 3220–3234, http://dx.doi.org/10.1175/MWR-D-11-00221.1.

[30] H. Jasak, Error Analysis and Estimation for the Finite Volume Method with Applications to Fluid Flows, Imperial College London (University of London), 1996.

[31] E. Robertson, V. Choudhury, S. Bhushan, D.K. Walters, Validation of OpenFOAM numerical methods and turbulence models for incompressible bluff body flows, Comput. & Fluids 123 (2015) 122–145, http://dx.doi.org/10.1016/j.compfluid.2015.09.010.

[32] S.V. Patankar, D.B. Spalding, A calculation procedure for heat, mass and momentum transfer in three-dimensional parabolic flows, Int. J. Heat Mass Transfer 15 (10) (1972) 1787–1806, http://dx.doi.org/10.1016/0017-9310(72)90054-3.

[33] R.I. Issa, Solution of the implicitly discretised fluid flow equations by operator-splitting, J. Comput. Phys. 62 (1) (1986) 40–65, http://dx.doi.org/10.1016/0021-9991(86)90099-9.

[34] J. Sauer, G.H. Schnerr, Unsteady cavitating flow-a new cavitation model based on a modified front capturing method and bubble dynamics, in: Proceedings of 2000 ASME Fluid Engineering Summer Conference, vol. 251, 2000, pp. 1073–1079.

[35] J. Sauer, Instationär kavitierende Strömungen - Ein neues Modell, basierend auf Front Capturing (VoF) und Blasendynamik, 2000, http://dx.doi.org/10.5445/IR/3122000.

[36] G.H. Schnerr, J. Sauer, Physical and numerical modeling of unsteady cavitation dynamics, in: Fourth International Conference on Multiphase Flow, vol. 1, ICMF New Orleans New Orleans, LO, USA, 2001.

[37] P.E. Farrell, J.R. Maddison, Conservative interpolation between volume meshes by local Galerkin projection, Comput. Methods Appl. Mech. Engrg. 200 (1) (2011) 89–100, http://dx.doi.org/10.1016/j.cma.2010.07.015.

[38] H.J. Aguerre, S. Márquez Damián, J.M. Gimenez, N.M. Nigro, Conservative handling of arbitrary non-conformal interfaces using an efficient supermesh, J. Comput. Phys. 335 (2017) 21–49, http://dx.doi.org/10.1016/j.jcp.2017.01.018.

[39] F. Avellan, Introduction to cavitation in hydraulic machinery, in: Scientific Bulletin of the Politehnica University of Timisoara: Transactions on Mechanics, Timisoara, Romania, 2004.

[40] Z. Fei, R. Zhang, H. Xu, J. Feng, T. Mu, Y. Chen, Energy performance and flow characteristics of a slanted axial-flow pump under cavitation conditions, Phys. Fluids 34 (3) (2022) 035121, http://dx.doi.org/10.1063/5.0085388.

[41] J. Feng, N. Zhao, G. Zhu, G. Wu, Y. Li, X. Luo, Cavitation identification in a hydraulic bulb turbine based on vibration and pressure fluctuation measurements, Mech. Syst. Signal Process. 208 (2024) 111042, http://dx.doi.org/10.1016/j.ymssp.2023.111042.

[42] B. Schiavello, F.C. Visser, Pump cavitation: Various NPSHR criteria, NPSHA margins, impeller life expectancy, in: Proceedings of the 25th International Pump Users Symposium, 2009, pp. 113–144, http://dx.doi.org/10.21423/R1XM30.

[43] R. Laborde, P. Chantrel, M. Mory, Tip clearance and tip vortex cavitation in an axial flow pump, J. Fluids Eng. 119 (3) (1997) 680–685, http://dx.doi.org/10.1115/1.2819298.

[44] P.J. Schmid, Dynamic mode decomposition of numerical and experimental data, J. Fluid Mech. 656 (2010) 5–28, http://dx.doi.org/10.1017/S0022112010001217.

[45] M.R. Jovanović, P.J. Schmid, J.W. Nichols, Sparsity-promoting dynamic mode decomposition, Phys. Fluids 26 (2) (2014) 024103, http://dx.doi.org/10.1063/1.4863670.